

See discussions, stats, and author profiles for this publication at: <https://www.researchgate.net/publication/231169219>

Measurement of particle density, porosity, and size distributions by sedimentation/steric field-flow fractionation: application to chromatographic supports', Anal. Chem. 63, 2869-2...

ARTICLE in ANALYTICAL CHEMISTRY · DECEMBER 1991

Impact Factor: 5.64 · DOI: 10.1021/ac00024a013

CITATIONS

32

READS

14

2 AUTHORS, INCLUDING:



Myeong Hee Moon

Yonsei University

150 PUBLICATIONS 2,408 CITATIONS

SEE PROFILE

injection end of the column. Consequently, the electric field strength at the injection point will become stronger and stronger until the water plug is completely out of the column. Once the water plug is gone, the field strength at the injection point will drop to the normal value and the negative ions will then be carried out of the column from the injection end by the electroosmotic flow. This is probably the reason for the sudden deviation of our last data point from the theoretical predication.

So far it has been assumed that the effect of the sample ions on the conductivity of the water plug and the column buffer is negligible. This is usually true for sample concentrations less than 10^{-5} M. For higher sample concentrations, the field enhancement factor will be reduced and one obviously has to take that into account. In addition, it has been assumed that the conductivity of the water plug and the sample buffer are constant during sample injection. This is obviously not true, as the migration of coions and counterions will cause a change in the conductivity or pH and further complicate our model. Some complicated samples might be very sensitive to these changes in the buffer condition. A full-scale computer simulation is then necessary to perform an accurate calculation (16-19).

LITERATURE CITED

- (1) Jorgenson, J. W.; Lukacs, K. D. *Anal. Chem.* **1981**, *53*, 1298.
- (2) Mikkers, F. E. P.; Everaerts, F. M.; Verheggen, Th. P. E. M. *J. Chromatogr.* **1979**, *169*, 1.
- (3) Kuhr, W. G. *Anal. Chem.* **1990**, *62*, 403R.
- (4) Dolnik, V.; Cobb, K. A.; Novotny, M. *J. Microcolumn Sep.* **1990**, *2*, 127.
- (5) Foret, F.; Sustacek, V.; Boček, P. *J. Microcolumn Sep.* **1990**, *2*, 229.
- (6) Everaert, F. M.; Verheggen, Th. P. E. M.; Mikkers, F. E. P. *J. Chromatogr.* **1979**, *169*, 21.
- (7) Moring, S. E.; Colburn, J. C.; Grossman, P. D.; Lauer, H. H. *LC-GC* **1989**, *8*, 34.
- (8) Burgi, D. S.; Chien, R.-L. *J. Microcolumn Sep.* **1991**, *3*, 199.
- (9) Chien, R.-L.; Burgi, D. S. *J. Chromatogr.* **1991**, *559*, 141.
- (10) Hjertén, S.; Jerstedt, S.; Tiselius, A. *Anal. Biochem.* **1965**, *11*, 219.
- (11) Gross, L.; Yeung, E. S. *J. Chromatogr.* **1989**, *480*, 169.
- (12) Lauer, H. H.; McManigill, D. *Anal. Chem.* **1986**, *58*, 166.
- (13) Chien, R.-L.; Burgi, D. S. *J. Chromatogr.* **1991**, *559*, 153.
- (14) Chien, R.-L.; Helmer, J. C. *Anal. Chem.* **1991**, *63*, 1354.
- (15) Huang, X.; Gordon, M. J.; Zare, R. N. *Anal. Chem.* **1988**, *60*, 377.
- (16) Bier, M.; Paluszinski, O. A.; Mosher, R. A.; Saville, D. A. *Science* **1983**, *219*, 1281.
- (17) Mosher, R. A.; Dewey, D.; Thormann, W.; Saville, D. A.; Bier, M. *Anal. Chem.* **1989**, *61*, 362.
- (18) Roberts, G. O.; Rhodes, P. H.; Snyder, R. S. *J. Chromatogr.* **1989**, *480*, 35.
- (19) Dose, E. V.; Gulochon, G. A. *Anal. Chem.* **1991**, *63*, 1063.

RECEIVED for review June 18, 1991. Accepted September 25, 1991.

Measurement of Particle Density, Porosity, and Size Distributions by Sedimentation/Steric Field-Flow Fractionation: Application to Chromatographic Supports

J. Calvin Giddings* and Myeong Hee Moon

Field-Flow Fractionation Research Center, Department of Chemistry, University of Utah, Salt Lake City, Utah 84112

A procedure is developed here for measuring the density and density distribution of polydisperse populations of near-spherical particles having diameters $>1 \mu\text{m}$ using a combination of sedimentation/steric (Sd/St) FFF and microscopy. This procedure is an extension of a recent calibration method designed to measure the size and size distribution of populations of particles of known density by Sd/StFFF using latex calibration standards. Both procedures are based on a density compensation principle in which particles of different densities are assumed to be retained identically if the field strength is adjusted to be inversely proportional to the density difference $\Delta\rho$ between particle and carrier. Following the development of the new calibration procedure, the above methods are applied to a group of five porous silicas used as chromatographic supports. The fractionation of the supports into narrow size classes by Sd/StFFF is demonstrated by the electron microscopy of collected fractions. Seven sizes (4-29 μm) of polystyrene latex particles are chosen for calibration. Values of diameter and $\Delta\rho$ selectivities generally fall in the ranges 0.72-0.77 and 0.15-0.25, respectively. By positioning retention time (from Sd/StFFF) and particle diameter (from microscopy) data for different silica fractions on the calibration plots, the density and thus the specific pore volume V_p of each fraction can be determined. The data suggest a small increase in V_p with size, which may be due in part to system band broadening. The average V_p values, unaffected by band broadening, are in reasonable agreement with those from outside sources.

* Corresponding author.

The distribution of any uniform particle population—either submicron or above in size—across the transverse (thin) coordinate of a field-flow fractionation (FFF) channel depends on the field-induced driving force exerted on the particles (1, 2). The relative downstream migration velocity (and thus the retention time) of the particles is determined by this transverse distribution and consequently by the driving force. In sedimentation FFF, the magnitude of the driving force is dependent on both particle size and particle density. The resulting association between retention time and size-density parameters can—if well understood and properly utilized—yield size and density distribution information about particle samples. The ability to acquire particle mass, size, and density data from SdFFF has been long recognized (3, 4). Experimentally, size characterization was realized at a relatively early date (4); the acquisition of particle density values is more recent and has been limited to submicron particle distributions (5-8).

We report here the development of a new strategy by which density and density distribution information can be acquired for supramicron ($>1 \mu\text{m}$) size spherical (or near-spherical) particles using a combination of sedimentation/steric FFF (Sd/StFFF) and microscopy. The strategy is applied to chromatographic support materials. The effective density of such particles is a function of particle porosity, an important parameter underlying chromatographic performance. We will demonstrate the methodology developed here by measuring the porosity and pore volume of several chromatographic supports.

The capability of the steric form of sedimentation FFF (Sd/StFFF) to separate particles larger than $1 \mu\text{m}$ in diameter

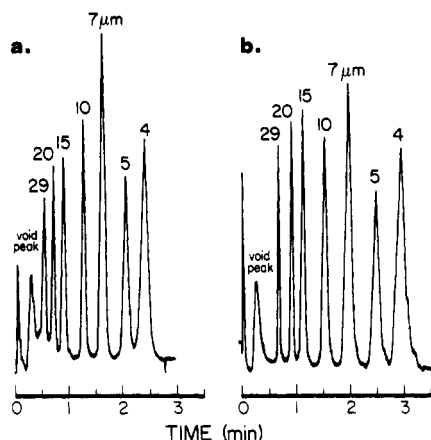


Figure 1. Effect of field strength (and thus of density increment $\Delta\rho$) on retention in sedimentation/steric FFF. The retained components are polystyrene latex microspheres of the indicated diameters. The separation in part a was induced by a rotation rate of 750 rpm while that in b was achieved at 1500 rpm. The flow rate in both cases was 6.0 mL/min.

according to size has been recognized since the inception of the steric operating mode of FFF (9). Since that time, major advances have been made in understanding and controlling the Sd/StFFF separation (10–12), making it possible to achieve particle fractionation at both high speed and high resolution (see Figure 1). However, the improved understanding contradicts the original view that particle retention and separation is dependent *only* on particle size and independent of parameters such as density. (This view, in fact, was shortlived since the separation of particles based on density was reported as early as 1979 (10).)

It has become increasingly clear that the transport of particles toward the wall by the primary driving force in Sd/StFFF is opposed by hydrodynamic lift forces. The equilibrium position (or distribution) of particles in the vicinity of the wall is consequently dependent upon the magnitude of the driving force acting in opposition to the lift forces. When the driving force is sedimentation, then its magnitude assumes a dependence upon particle density and the retention time becomes density dependent. More specifically, the sedimentation force for like-sized particles is proportional to the product $G\Delta\rho$ where G is the strength of the sedimentation field measured as acceleration and $\Delta\rho$ is the difference in the density of the particle and the liquid in which it is suspended (12). Thus retention time t_r depends on $G\Delta\rho$. Because both the driving force and t_r are dependent upon the product of these two terms, changes in either one will have an equivalent effect on retention. (This conclusion is based on the assumption, justified both by our experience (12) and by theory (13), that lift forces are independent of particle density.) Figure 1 shows how the fractogram (elution profile) of polystyrene latex beads is influenced by a 4-fold change in G (corresponding to a doubling of system rpm). A like change will be generated by a 4-fold difference in $\Delta\rho$.

The dependence of retention on the product $G\Delta\rho$ applies to both the normal and steric modes of sedimentation FFF. That is, it applies to both submicron-sized particles (normal FFF) and supramicron-sized particles (steric FFF). However, procedures for obtaining density information have been simpler to develop for normal FFF because the theory of normal FFF is relatively straightforward and explicit equations can be derived showing the dependence of retention upon $G\Delta\rho$ and on particle diameter d (5). Steric FFF, by contrast, is complicated by the hydrodynamic lift forces, which are not well understood (13). However, calibration procedures have been developed recently that make it possible to acquire accurate size distribution data from Sd/StFFF runs (12). These

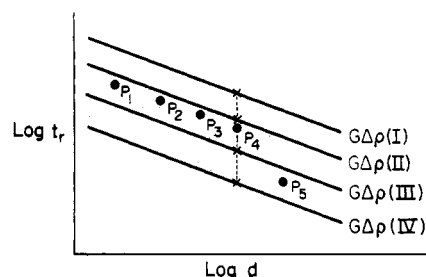


Figure 2. Schematic representation (slanted lines) of the calibration plots obtained for different values of $G\Delta\rho$. The points labeled P_1 through P_5 are established experimentally for the collected fractions of the sample to be characterized. The densities of each fraction, and thus the density distribution of the sample, can be obtained by plotting $\log t_r$ versus $\log G\Delta\rho$ using values obtained from the vertical line passing through the successive points. One such vertical line passing through data point number 4 is shown in the figure.

calibration procedures are extended in this work in such a way that density parameters can be obtained as well. In contrast to the procedures developed for sedimentation/normal FFF, it is not necessary to obtain several fractograms at different carrier densities. Instead, our current procedure relies on an auxiliary method for measuring particle diameter. In particular, to obtain a density distribution, the average particle diameter of each of a number of fractions collected from the effluent stream of the sedimentation FFF system must be accurately determined. Since the collected particles of interest are relatively large and readily measured by optical microscopy, the optical microscope can be used to provide the adjunct size information. In these studies we have used both optical and electron microscopy. Other accurate methods for size determination could be used as well including flow FFF.

CALIBRATION PROCEDURE

It has been established empirically that a plot of the logarithms of the retention time t_r versus the particle diameter d approximates a straight line over a considerable diameter range at a fixed value of $G\Delta\rho$ (12). Other straight lines are generated for other values of $G\Delta\rho$. These plots are represented schematically in Figure 2. Each plot is associated with a specific value of $G\Delta\rho$ designated as $G\Delta\rho(I)$, $G\Delta\rho(II)$, ..., where $G\Delta\rho(I) > G\Delta\rho(II)$, and so on. These plots are established readily using well-characterized particles such as polystyrene latex beads for which $\Delta\rho = 0.050$ g/mL. The different plots are generated by working at different spin rates and thus different G values in a sedimentation FFF apparatus.

In an earlier paper it was shown that such calibration plots can be used to obtain the accurate size distribution of spherical particles of arbitrary (but known) density (12). The procedure involves adjusting the G of the centrifuge such that the product $G\Delta\rho$ for the sample material is the same as that used to produce one of the polystyrene calibration curves. The results of this procedure are in good agreement with those produced by microscopic examination (12).

For particles of unknown density, the procedure is different but is based on the same principles. In order to obtain a density distribution, fractions are collected across the sample peak. (Each fraction yields one density value.) The retention time t_r of each fraction is recorded. The mean diameter d of particles in the fraction is then established by microscopy or other means. In this way, a value of t_r and d is established for each fraction. The points corresponding to these fractions are then plotted on the $\log t_r$ versus $\log d$ calibration graph. Five such points are shown schematically in Figure 2. If the points lie between two specific plots such as $G\Delta\rho(II)$ and $G\Delta\rho(III)$, as is the case for points 1–4 in Figure 2, then the $G\Delta\rho$ value will be intermediate between these two specific values of $G\Delta\rho$. Since G for the experiment is controlled ex-

perimentally, this establishes the $\Delta\rho$ range in which the different particle fractions fall. If density varies with particle diameter, then we will find points shifting up or down relative to the calibration plots. Thus point 5 is shown to lie below the $G\Delta\rho$ (III) but above the $G\Delta\rho$ (IV) plot, signifying that the particles in fraction 5 have a lower density than those in fractions 1–4.

In order to establish the actual value of the $\Delta\rho$ of a fraction instead of merely finding the range of $\Delta\rho$'s in which it lies, a second plot is made. This is a plot of $\log t_r$ versus $\log G\Delta\rho$ at the specific diameter of particles in the fraction being examined. Thus in the case of Figure 2, one such plot would be obtained by plotting the four points shown by the crosses lying on the vertical dashed line corresponding to the diameter observed for fraction 4. Similar plots can be made for the other fractions. When plotted, all these lines are also found to be nearly straight (although this is not critical to the procedure) and the precise $G\Delta\rho$ value for each fraction can be read from the graph. With the G of the experiment known, a specific value of $\Delta\rho$ is immediately calculated. We note that by this procedure, $\Delta\rho$ is measured independently for every fraction. Thus, in principle, any variation of $\Delta\rho$ with particle diameter can be readily determined, thus yielding a form of the density distribution and not just the average density. However, as we explain later, any trend found for density variation with size for narrow size distributions is distorted somewhat by band-broadening effects.

If it is reasonable to assume that all density values are the same, independent of particle diameter, then to obtain that density it will suffice to (1) determine $\Delta\rho$ for only one fraction, preferably at the peak maximum, or (2) obtain $\Delta\rho$ for several fractions and calculate an average value. In case 1 the microscopy is particularly simple because one need only determine the average diameter of a fraction whose diameter range is made very narrow by the fractionation process.

SELECTIVITY

The diameter selectivity S_d is defined by either of two equivalent expressions

$$S_d = |d \log t_r / d \log d| = |d \ln t_r / d \ln d| \quad (1)$$

and is thus equal to the absolute value of the slope of the calibration plots. Parameter S_d reflects the rate of change of t_r with respect to d (under constant experimental conditions) and thus the effectiveness of the separation of particles having different d values. The logarithmic form conveniently measures relative changes as seen by writing $d \log x = (1/2.303) dx/x$ for any variable x . Thus

$$S_d = \left| \frac{dt_r/t_r}{dd/d} \right| \quad (2)$$

Since the percentage change in t_r (or d) is simply $100 dt_r/t_r$ (or $100 dd/d$), S_d becomes

$$S_d = |\text{percent change in } t_r / \text{percent change in } d| \quad (3)$$

Since t_r depends on particle density ρ_p (or density difference $\Delta\rho$) as well as d , we can similarly define a $\Delta\rho$ selectivity

$$S_{\Delta\rho} = |d \log t_r / d \log \Delta\rho| \quad (4)$$

reflecting the sensitivity of t_r to $\Delta\rho$ for fixed experimental conditions at a given d . Thus $S_{\Delta\rho}$ is the slope of the second calibration plot described above. The accuracy with which $\Delta\rho$ can be established by measuring changes in t_r clearly increases with $S_{\Delta\rho}$.

It is difficult to determine $S_{\Delta\rho}$ from eq 4 because of the absence of particle standards of fixed size but variable density. Instead, we utilize the fact that retention depends on the product $G\Delta\rho$ and that any change in G (which is easily con-

trolled) is equivalent to an equal fractional change in $\Delta\rho$. Thus

$$S_{\Delta\rho} = |d \log t_r / d \log G| \quad (5)$$

where the derivative is taken at a constant d and $\Delta\rho$ (and thus can be determined for a single particle standard) and at constant flow rate.

Some error will be found in measuring the average diameter for each particle fraction. This will introduce an error into the measurement of $\Delta\rho$. This error can be examined by looking at small changes in t_r caused by variations in d and $\Delta\rho$

$$d \log t_r = \frac{\partial \log t_r}{\partial \log d} d \log d + \frac{\partial \log t_r}{\partial \log \Delta\rho} d \log \Delta\rho \quad (6)$$

When errors in t_r are considered negligible, we write $d \log t_r = 0$ and thus obtain

$$\frac{\partial \log \Delta\rho}{\partial \log d} = \frac{-\partial \log t_r / \partial \log d}{\partial \log t_r / \partial \log \Delta\rho} = \frac{S_d}{S_{\Delta\rho}} \quad (7)$$

Since S_d for Sd/StFFF (generally 0.6–0.8) is several times larger than $S_{\Delta\rho}$ (which in these studies we find generally to be in the range 0.15–0.25), a few percentage error in d will be amplified several-fold in $\Delta\rho$. However, since $\rho_p = \rho + \Delta\rho$, where the density ρ of the carrier is accurately known, the relative error in ρ_p is reduced below that found for $\Delta\rho$, specifically

$$\frac{\partial \log \rho_p}{\partial \log d} = \frac{\Delta\rho}{\rho_p} \frac{S_d}{S_{\Delta\rho}} \quad (8)$$

Thus the relative error in ρ_p is reduced substantially below that in $\Delta\rho$; for chromatographic silica the ratio in eq 8 is about unity. Note that the error in ρ_p can be reduced by reducing $\Delta\rho$, in some cases achievable by altering the carrier density in the direction of the particle density. We observe also that errors in t_r will contribute to errors in $\Delta\rho$, as expressed by the final term of eq 6.

For Sd/StFFF, $dt_r/d\Delta\rho > 0$ and thus the absolute value designation of eq 4 can be removed. Integration of this equation over any region for which $S_{\Delta\rho}$ is substantially constant yields

$$S_{\Delta\rho} = \log(t_r/t_{r0}) / \log(\Delta\rho/\Delta\rho_0) \quad (9)$$

which can be rearranged to

$$t_r/t_{r0} = (\Delta\rho/\Delta\rho_0)^{S_{\Delta\rho}} \quad (10)$$

where t_{r0} and $\Delta\rho_0$ are any pair of reference values. Since changes in G and $\Delta\rho$ are equivalent, one can similarly integrate eq 5 to obtain

$$S_{\Delta\rho} = \log(t_r/t_{r0}) / \log(G/G_0) \quad (11)$$

DENSITY, POROSITY, AND PORE VOLUME

The *specific pore volume* (or simply *pore volume*) V_P is defined as the volume of pore space per unit mass of solid matrix; it is usually expressed in the units mL/g (14). Similarly, the *specific solid volume* V_S can be defined as the volume of the solid material per unit solid mass, or simply $1/\rho_S$, where ρ_S is the density of the solid. The apparent density ρ_{app} of a porous particle is given by the weighted average of ρ_S and ρ'

$$\rho_{app} = \frac{\rho' V_P + \rho_S V_S}{V_P + V_S} \quad (12)$$

where ρ' is the density of the fluid (if any) occupying the pore

Table I. Chromatographic Supports Used in This Study

support	supplier	batch no.	pore size, Å	V_p , mL/g	surface area, m ² /g
(a) Nucleosil	Machery-Nagel	5121	120	0.7	180
(b) Hypersil-5	Shandon	5-148R	120	0.61	175
(c) Hypersil-5	Shandon		136	0.56	144
(d) Spherisorb	Phase Separations		80		190
(e) Hypersil-3	Shandon	3-51	120	0.63	185

space. (In most cases ρ' equals ρ , the carrier density.) Since $V_s = 1/\rho_s$, we obtain

$$\rho_{app} = \frac{\rho' V_p + 1}{V_p + 1/\rho_s} \quad (13)$$

Upon solving for V_p we get

$$V_p = \frac{1}{\rho_s} \frac{\rho_s - \rho_{app}}{\rho_{app} - \rho'} \quad (14)$$

If the pores are occupied by water then ρ' is 0.997 g/mL at room temperature.

The particle porosity ϵ is simply the fraction of the particle volume occupied by pores

$$\epsilon = \frac{V_p}{V_p + V_s} \quad (15)$$

The apparent density expressed in terms of ϵ is

$$\rho_{app} = \epsilon \rho' + (1 - \epsilon) \rho_s \quad (16)$$

which yield ϵ in terms of ρ_{app}

$$\epsilon = \frac{\rho_s - \rho_{app}}{\rho_s - \rho'} \quad (17)$$

EXPERIMENTAL SECTION

Apparatus. The basic sedimentation FFF system used in this work is nearly identical to the Model S101 Colloid/Particle Fractionator from FFFractionation, Inc. (Salt Lake City, UT). A special channel of reduced dimensions was used in this system; this channel has a breadth b of 1.0 cm, a thickness w of 127 μ m, and a tip-to-tip length L of 90.0 cm. The void volume as measured by the nonretained volume of a sodium benzoate peak is 1.4 mL. The radius of rotation is 15.1 cm.

An HPLC pump, Kontron Model 410 (Kontron Electrolab, London, U.K.), was used for the channel flow. Another pump, the FMI Lab Pump Model QD-2 (Fluid Metering, Inc., Oysterbay, NY), was used for flushing the channel at high speed (about 30 mL/min) after every silica run in order to avoid contamination of the channel. A Spectroflow Monitor SF770 (Kratos Analytical Instruments, Westwood, NJ) UV-visible detector was used (at 300-nm wavelength) to monitor the eluted samples. A strip chart recorder from Houston Instrument Corp. (Austin, TX) was used for recording. Fractions of eluted silica particles were collected using a Model FC-80K Microfractionator from Gilson Medical Electronics (Middletown, WI).

Reagents and Samples. The carrier liquid was doubly distilled and deionized water containing 0.1% (v/v) FL-70 detergent (Fisher Scientific, Fairlawn, NJ) and 0.02% (w/v) sodium azide as a bactericide. For calibrating the system, polystyrene particle standards (Duke Scientific, Palo Alto, CA) with nominal diameters of 29.4, 19.58, 15.00, 9.87, 7.04, 5.002, and 3.983 μ m were used. (Hereafter these standards are described by the diameter designations 29, 20, 15, 10, 7, 5, and 4 μ m, respectively.) The chromatographic supports used in this study are tabulated in Table I.

Procedure. The silica samples were suspended with the carrier liquid and sonicated for at least 6 h to assure the replacement of the air in the pores with the carrier liquid. Sample volumes of 4–5 μ L of 15 mg/mL silica suspensions were injected directly into the channel. The carrier flow was then interrupted and the centrifuge started spinning. When the centrifuge reached the

Table II. Calculation of Density Selectivity $S_{\Delta\rho}$ from Retention Times of Figure 1 for Polystyrene Standards of Different Diameters d Using Eq 11

d , μ m	t_{r0} , min ^a	t_r , min ^b	t_r/t_{r0}	$S_{\Delta\rho}$
4	2.37	2.94	1.24	0.155
5	2.02	2.51	1.24	0.157
7	1.57	1.98	1.26	0.167
10	1.23	1.55	1.26	0.167
15	0.87	0.14	1.31	0.195
20	0.67	0.93	1.38	0.237
29	0.51	0.68	1.33	0.208

^a From Figure 1a, 750 rpm. ^b From Figure 1b, 1500 rpm.

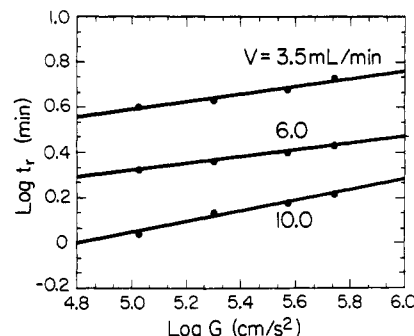


Figure 3. Plots of $\log t_r$ versus $\log G$ for 5- μ m latex at different flow rates. The slopes of the lines equal the density selectivities $S_{\Delta\rho}$, which are compiled for these and other plots in Table III.

desired rpm, the flow was resumed. It took ~ 30 – 40 s to reach 434 rpm, a time more than sufficient to achieve the relaxation of the silica particles. All experiments were carried out at the ambient laboratory temperature, 296 \pm 0.5 K.

Microscopy. A Hitachi (Nissei Sangyo America, Mountain View, CA) S-450 scanning electron microscope (SEM) was used to obtain electron micrographs of fractions of supports a and e, Table I. Particles from the fraction collector were taken by disposable pipet and placed on a 13-mm Nucleopore (Pleasanton, CA) membrane filter having 0.1- μ m pores. This filter was mounted on a steel stub with a colloidal graphite adhesive (Ted Pella Corp., Redding, CA), and the filter surface was coated with a gold and palladium mixture in a 60/40 ratio. The SEM was set at 20 kV and 750–1000 \times magnification. Size measurements were made to within 0.2 μ m with a magnifier. The diameters of 40–60 particles were measured for each fraction. Irregular particles, such as those found in the early fractions of Hypersil-3 (support e in Table I), were not counted for size measurement.

RESULTS AND DISCUSSION

An initial value of the density selectivity $S_{\Delta\rho}$ can be obtained by applying eq 11 to the two fractograms shown in Figure 1. For this case $G/G_0 = 4$. The retention time ratio t_r/t_{r0} observed upon going from the lower field run (Figure 1a) to the higher field run (Figure 1b) can be obtained from the fractograms. The results are shown in Table II. The $S_{\Delta\rho}$ values calculated from the t_r/t_{r0} ratios are seen to be fairly consistent among the various polystyrene standards, ranging from 0.16 to 0.24, with a slight tendency to increase with increasing particle size. While these selectivities are relatively low for FFF, they are generally higher than the mass selectivity used for molecular weight analysis in size exclusion chromatography and they are thus adequate to accurately discern small differences in density.

Since the value of $S_{\Delta\rho}$ is crucial to our analysis, we have investigated the effect of flow rate on this parameter. For this purpose, we have developed plots of $\log t_r$ versus $\log G$ for a group of particle sizes (3, 5, 7, and 10 μ m) at three different flow rates. The results for the 5- μ m latex are shown in Figure 3. At each of the flow rates the points appear to be aligned in a nearly straight line. (A least-squares straight line is shown

Table III. Values of $S_{\Delta\rho}$ for Four Diameters of Latex Standards at Three Different Flow Rates^a

$d, \mu\text{m}$	flow rate, mL/min		
	3.5	6.0	10.0
10	0.162	0.163	0.390
7	0.165	0.154	0.311
5 ^b	0.169	0.145	0.237
3	0.173	0.132	0.123

^aThe G range is from 108.1 to 562.8 gravities. ^bPlotted in Figure 3.

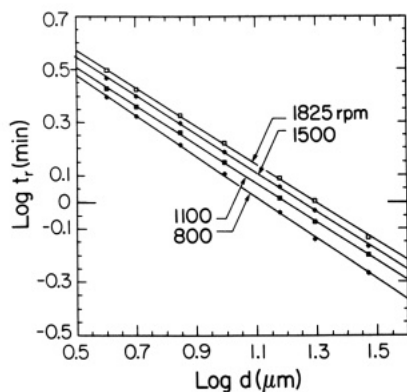


Figure 4. Log t_r versus log d calibration plots obtained from the seven polystyrene latex standards at different rotation rates. The data points used to construct the plots are shown. The flow rate \dot{V} for all experiments was 6.0 mL/min.

for each flow rate.) The density selectivity, equal to the slope of the line, is shown for each of the flow rates (and for each diameter) in Table III. We see that, in general, $S_{\Delta\rho}$ increases with flow rate.

While we have plotted the data in Figure 3 on a straight line basis, we note that the actual points for the upper plot could be better fit to a curve that is concave up. Conversely, the points for the lower plot suggest a concave down configuration. The plots for the other particle diameters (not shown) verify this trend. Most of our work has been done at 6.0 mL/min, which yields a better straight line relationship. Clearly, however, a straight line is not required for calibration as long as the calibration plot can be well defined by the latex standards.

We now proceed to evaluate the density of some chromatographic supports. To this end we use the latex standards (assumed density 1.050 g/mL) to construct a set of diameter-based selectivity plots like those illustrated schematically in Figure 2. The experimental results, generated at a flow rate of $\dot{V} = 6.0$ mL/min and at different rpm values, are shown in Figure 4. (We note that the 1500 rpm plot is based on data taken from Figure 1b.) The rpm values shown in the figure combined with the centrifuge radius and the density difference of latex and aqueous carrier (0.053 g/mL) can be used to calculate $G\Delta\rho$ values for each rpm. The data related to Figure 4 are summarized in Table IV. We observe that the data adhere relatively closely to a straight line plot over the 7.3-fold diameter range (4–29 μm) of the latex standards.

The fractogram of the Nucleosil (a, Table I) support material obtained at 434 rpm and $\dot{V} = 6.0$ mL/min is shown in Figure 5. The peak, of course, is broader than that of the latex standards because of the wider distribution of particle sizes. The width of the peak provides a measure of the breadth of the size distribution provided particle densities do not vary significantly with size.

In accordance with our discussion in the Calibration Procedure, fractions (of volume 0.6 mL) were collected at discrete time intervals as the support material emerged from the FFF

Table IV. Experimental Conditions and Parameters Corresponding to Calibration Plots of Figure 4^a

rpm	$10^{-4}G\Delta\rho, \text{g}/(\text{cm}^2 \text{ s}^2)$	S_d	t_{r1}, min^b	cc^c
1825	2.92	0.721	8.58	1.000
1500	1.97	0.729	8.13	1.000
1100	1.06	0.729	7.42	1.000
800	0.562	0.768	7.27	0.999

^aAll flow rates = 6.0 mL/min. ^bRetention time of 1- μm particle (the extrapolated intercept on the log t_r axis). ^cCorrelation coefficient for plot.

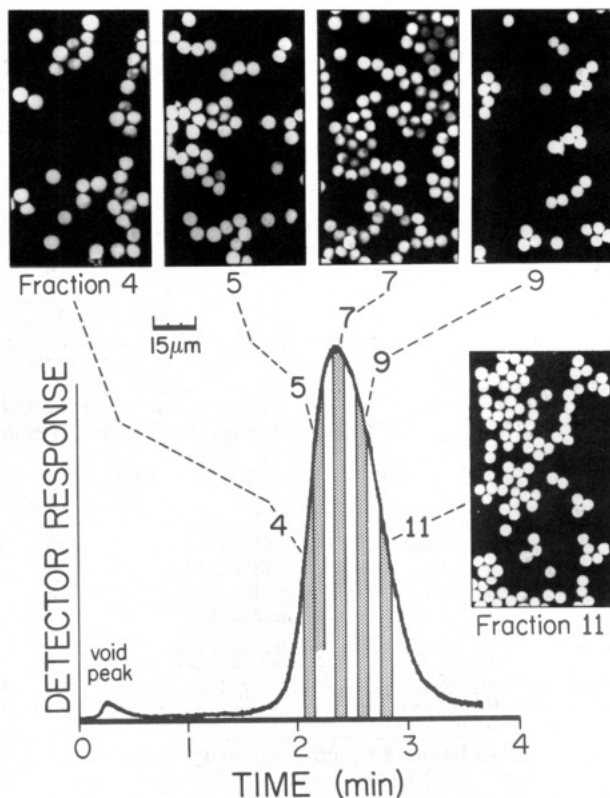


Figure 5. Fractogram of Nucleosil showing the position of the collected fractions. Electron micrographs obtained for each fraction are shown.

channel. We focus here on fractions 4, 5, 7, 9, and 11; the position at which these fractions were collected is shown in Figure 5. These fractions were examined by electron microscopy. Representative micrographs of the five fractions are shown in the figure. The average diameter clearly decreases upon proceeding from fraction 4 (5.91 μm) through fraction 11 (4.12 μm), showing that the sample is successfully fractionated by the FFF process. The diameters of the particles in each fraction were then determined from the micrographs, as described in the Experimental Section. These diameters (and other data) are shown in Table V. The diameter and retention time data then make it possible to position the experimental points for each fraction on the calibration surface of Figure 4, as shown schematically in Figure 2. (The corresponding points for the silica fractions on Figure 4 are not shown.) Density calibration plots are then established using the points of interception of the vertical lines passing through the data points for the fractions with the calibration plots of Figure 4, as also shown schematically in Figure 2. The resulting density-based calibration plots are shown in Figure 6. The experimental points for the fractions obtained by using the observed retention time (actually the midpoint time of collection of the fraction) as it falls on the corresponding calibration plot are also shown in the figure. Each of the points so obtained are clearly associated with a

Table V. Calculated Apparent Density, Specific Pore Volume, and Porosity of the Collected Fractions for Nucleosil (Support a in Table I) As Shown in Figure 5a^a

fraction no.	t_r , min	d , μm	$10^{-4}G\Delta\rho$, g/(s ² cm ²)	$\Delta\rho$, g/cm ³	ρ_{app} , g/cm ³	V_p , mL/g	ϵ
4	2.08–2.18	5.91 ± 0.31^b	1.42	0.45	1.45	0.75	0.62
5	2.18–2.28	5.66 ± 0.29	1.56	0.50	1.50	0.64	0.58
7	2.38–2.48	4.92 ± 0.29	1.39	0.45	1.44	0.77	0.63
9	2.58–2.68	4.55 ± 0.20	1.61	0.52	1.52	0.60	0.57
11	2.78–2.88	4.12 ± 0.21	1.62	0.52	1.52	0.60	0.57
av values					1.48 ± 0.03	0.67 ± 0.08	0.60 ± 0.03

^a All calculations based on an assumed density (ρ_s) of nonporous silica of 2.20 g/cm³. ^b Mean and standard deviation based on ~ 50 particle diameter measurements.

Table VI. Calculated Apparent Density, Specific Pore Volume, and Porosity of the Fractions of Hypersil-3 (Support e in Table I) As Shown in Figure 7^a

fraction no.	t_r , min	d , μm	$10^{-4}G\Delta\rho$, g/(s ² cm ²)	$\Delta\rho$, g/cm ³	ρ_{app} , g/cm ³	V_p , mL/g	ϵ
6	2.69–2.89	4.13 ± 0.22	1.48	0.48	1.47	0.69	0.60
8	3.09–3.29	3.48 ± 0.17	1.58	0.51	1.50	0.63	0.58
10	3.49–3.69	2.99 ± 0.15	1.66	0.53	1.53	0.57	0.56
12	3.89–4.09	2.60 ± 0.11	1.71	0.55	1.54	0.55	0.55
14	4.29–4.49	2.31 ± 0.31	1.84	0.59	1.59	0.47	0.51
av values					1.53 ± 0.04	0.58 ± 0.07	0.56 ± 0.03

^a All calculations based on an assumed density of nonporous silica of 2.20 g/cm³.

Table VII. Calculated Apparent Density, Specific Pore Volume, and Porosity of the Fractions of Hypersil-5 (Support b in Table I) ($V_p = 0.61$ mL/g) Resulting from a Run at 434 rpm and 6.0 mL/min^a

fraction no.	t_r , min	d , μm	$10^{-4}G\Delta\rho$, g/(s ² cm ²)	$\Delta\rho$, g/cm ³	ρ_{app} , g/cm ³	V_p , mL/g	ϵ
5	1.82–1.92	7.15 ± 0.29	1.51	0.49	1.48	0.67	0.60
6	1.92–2.02	6.55 ± 0.29	1.40	0.45	1.45	0.77	0.63
8	2.12–2.22	5.98 ± 0.30	1.70	0.55	1.54	0.55	0.54
10	2.32–2.42	5.39 ± 0.26	1.85	0.59	1.59	0.47	0.51
11	2.42–2.52	5.02 ± 0.51	1.72	0.55	1.55	0.54	0.54
av values					1.52 ± 0.05	0.60 ± 0.11	0.56 ± 0.04

^a All calculations based on an assumed density of nonporous silica of 2.20 g/cm³.

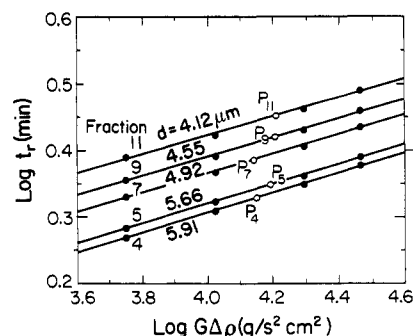
Table VIII. Calculated Apparent Density Specific Pore Volume, and Porosity of Fractions of Hypersil-5 (Support c in Table I) ($V_p = 0.56$ mL/g) Using Conditions Reported in Table VII^a

fraction no.	t_r , min	d , μm	$10^{-4}G\Delta\rho$, g/(s ² cm ²)	$\Delta\rho$, g/cm ³	ρ_{app} , g/cm ³	V_p , mL/g	ϵ
3	1.58–1.68	8.54 ± 0.34	1.45	0.46	1.46	0.72	0.61
5	1.78–1.88	7.46 ± 0.35	1.61	0.52	1.51	0.61	0.57
7	1.98–2.08	6.62 ± 0.31	1.71	0.57	1.57	0.50	0.52
9	2.18–2.28	5.87 ± 0.30	1.87	0.60	1.60	0.46	0.50
11	2.38–2.48	5.16 ± 0.31	1.77	0.57	1.56	0.51	0.53
13	2.58–2.68	4.70 ± 0.31	1.91	0.61	1.61	0.44	0.49
av values					1.55 ± 0.05	0.54 ± 0.10	0.54 ± 0.04

^a All calculations based on an assumed density of nonporous silica of 2.20 g/cm³.

specific $G\Delta\rho$ value. These values are shown in Table V. Since G is known, $\Delta\rho$ for each fraction can be obtained, as shown also in Table V. The apparent density ρ_{app} is then obtained by adding the density of the aqueous carrier (0.997 g/mL) to $\Delta\rho$, assuming that the pores are totally filled with the carrier. This result is shown in Table V along with values of the specific pore volume V_p calculated from eq 14 and the porosity from eq 17. The results suggest that there might be a small drift in pore volume and porosity with particle diameter, the larger particles tending to have the highest values of pore volume and porosity. A part of this trend may be an experimental artifact, as explained below.

The same procedure was followed for the Hypersil-3 support material. In this case seven fractions were collected and examined, as shown in Figure 7. A large number of irregular particles are shown in the micrographs of this support, particularly for the large-sized (early) fractions. Since only

**Figure 6.** Density-based calibration plots corresponding to the mean diameters of the five fractions collected from the Nucleosil sample.

spherical particles can be used for accurate calibration, fractions 3 and 4 were excluded from the procedure. The

Table IX. Calculated Apparent Density, Specific Pore Volume, and Porosity of Fractions of Spherisorb (Support d in Table I) Collected under Conditions Reported in Table VII^a

fraction no.	t_r , min	d μm	$10^{-4}G\Delta\rho$, g/(s ² cm ²)	$\Delta\rho$, g/cm ³	ρ_{app} , g/cm ³	V_p , mL/g	ϵ
4	1.85–1.95	7.48 ± 0.29	2.07	0.66	1.66	0.37	0.45
6	2.05–2.15	6.44 ± 0.30	1.96	0.63	1.63	0.42	0.48
9	2.35–2.45	5.47 ± 0.34	2.17	0.69	1.69	0.33	0.42
11	2.55–2.65	4.86 ± 0.31	2.08	0.67	1.67	0.36	0.45
13	2.75–2.85	4.45 ± 0.24	2.24	0.72	1.71	0.31	0.40
15	2.95–3.05	4.01 ± 0.26	2.14	0.69	1.68	0.34	0.43
av values					1.67 ± 0.03	0.36 ± 0.03	0.44 ± 0.02

^a All calculations based on an assumed density of nonporous silica of 2.20 g/cm³.

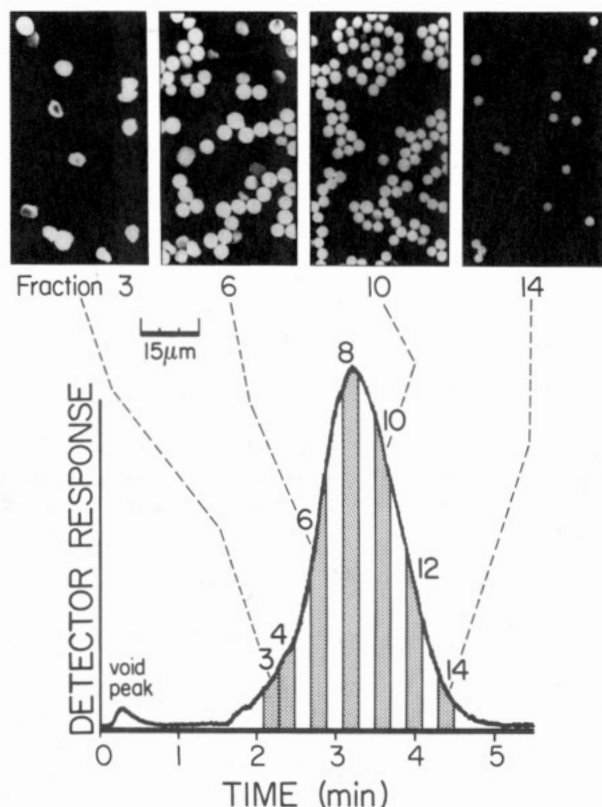


Figure 7. Fractogram of Hypersil-3 obtained at 434 rpm and $\dot{V} = 6.0$ mL/min. The position of the fraction utilized in this study are shown with the corresponding fraction number. Electron micrographs are shown for fractions 3, 6, 10, and 14.

density calibration plots for the other five fractions are shown in Figure 8. The resulting data are tabulated in Table VI. In the case of Hypersil-3, the tendency for the pore volume and porosity to decrease with decreasing particle diameter is even more pronounced than it is for Nucleosil.

Since the data of Tables V–IX suggest an unexpected decrease in particle density ρ_{app} and a corresponding increase in specific pore volume V_p with particle diameter d , it is useful to examine the possibility that this trend is generated by experimental error. We note first that any systematic errors in the measurement of particle diameter d would tend to give systematic errors in density without a significant trend. Random errors in d would likewise display no trend, but they have a bearing on the overall reliability of the results. A rough estimate of the effects of random variations in d can be made by noting that individual d values reported in Tables V–IX have a standard deviation of about 5%, which translates into an error of $\sim 0.7\%$ for the mean value of a typical 50 d measurements. From eq 8 the resulting random error in density, assuming $(\Delta\rho/\rho_p) = 1/3$, $S_d = 0.73$, and $S_{\Delta\rho} = 0.2$, is only $\sim 0.9\%$, of negligible significance compared to the observed variations in density. However, a 1% error in t_r for

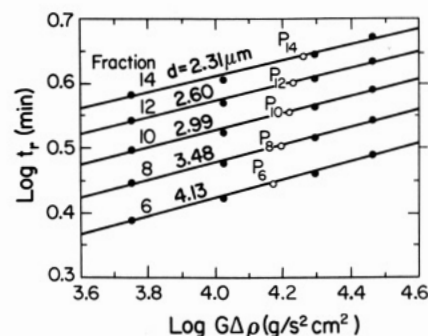


Figure 8. Density-based calibration plots for the five fractions of Hypersil-3 found to have spherical particles.

a given diameter will generate a 5% error in $\Delta\rho$ (see eq 6) and thus $\sim 1.6\%$ error in particle density. (We note that flow rate variations were a small fraction of 1% and thus did not contribute substantially to uncertainty in t_r .) These errors together, amounting to about 2%, are consistent with the random variation in reported particle density values.

Although the small random errors noted above in the measurement of d and t_r are not good candidates to explain the observed nonrandom variation of particle density with particle size, there is still another source of error to be considered that arises as a consequence of the narrow distribution (compared to most particle populations) of the chromatographic supports. Consider Figure 5. The particles collected in fraction 4 will not only include particles that belong in that precise interval but it will include some particles that have been transported into the interval corresponding to fraction 4 from adjacent intervals by the band-broadening processes in the channel. Since fraction 4 is collected from the leading edge of the distribution, more particles will contaminate that fraction from the right side (closer to the peak maximum) than from the left side where there are fewer particles. The particles to the right are smaller particles; thus the particles observed in fraction 4 will be somewhat smaller on average than belong there. This error in average d is equivalent to an error in t_r ; the smaller particles contaminating this fraction should be associated with a somewhat larger t_r value. This point P_4 in Figure 6 should be moved somewhat higher on the t_r axis which, if it is to remain on its same calibration line, would displace the point to the right along the $G\Delta\rho$ scale. Thus the measured density of this large particle fraction would be larger than that deduced from the data. By the same arguments, the fraction collected from the right hand side of the fractogram (e.g., fraction 11 in Figure 5) would be excessively contaminated by larger particles from the left, giving an error in the opposite direction. Thus point P_{11} in Figure 6 would be displaced somewhat to the left. These changes would tend to bring the densities of large and small particles closer together, thus eliminating much or all of the apparent trend in particle density and specific pore volume with diameter.

Table X. Comparison of the Pore Volume, Porosity, and Apparent Density of the Chromatographic Supports Obtained by FFF and Non-FFF Methods

support	non-FFF			FFF		
	ρ_{app}^a , g/cm ³	V_p , mL/g	ϵ	ρ_{app} , g/cm ³	V_p , mL/g	ϵ
(a) Nucleosil	1.47	0.7	0.61	1.48 ± 0.03	0.67 ± 0.08	0.60 ± 0.03
(b) Hypersil-5	1.51	0.61	0.57	1.52 ± 0.05	0.60 ± 0.11	0.56 ± 0.04
(c) Hypersil-5	1.54	0.56	0.55	1.55 ± 0.05	0.54 ± 0.10	0.54 ± 0.04
(d) Spherisorb				1.67 ± 0.03	0.36 ± 0.03	0.44 ± 0.02
(e) Hypersil-3	1.50	0.63	0.58	1.53 ± 0.04	0.58 ± 0.07	0.56 ± 0.03

^a Calculated from eqs 13 and 16.

A crude estimate of the order of magnitude of the above error can be given. For particles collected in a narrow fraction from a steep concentration gradient (as is the case for fractions 4 and 11 of Figure 5), the maximum expected t_r shift, δt_r , should be equal or less than the standard deviation σ in the elution time of the polystyrene latex standard of the same diameter obtained at the same $G\Delta\rho$ value. More specifically, for a particle population generating a near-Gaussian peak of standard deviation (in time) of σ_p , a narrow fraction collected at a time Δt relative to the peak maximum will have a δt_r given roughly by

$$\frac{\delta t_r}{t_r} = -\frac{\Delta t}{t_r} \frac{\sigma^2}{\sigma_p^2} \quad (18)$$

For standards having diameters of about 5 μm , the standard deviation σ relative to t_r is $\sim 2\%$ (see Figure 1). For fractions 4 and 11 we have $|\Delta t|/t_r \sim 0.2$ and $\sigma/\sigma_p \sim 0.15$. Thus $|\delta t_r|/\sigma \sim 0.2$ and $|\delta t_r|/t_r \sim 0.004$, an effective 0.4% shift in t_r . A 0.4% error in t_r , following the arguments given previously, should give $<1\%$ error in particle density. This percentage error does not appear to be large enough to explain the observed trends in particle density with particle diameter. This conclusion is based on the narrow peaks (Figure 1) obtained for the latex standards and assumes that monodisperse silica fractions would produce equally narrow peaks. It also ignores the effective band broadening stemming from the finite volumes of the fractions collected, which in the present case appears to contribute only slightly less than calculated above to δt_r . (The $\sim 5\%$ standard deviation in d reported in Table V for silica is not entirely explained by these band-broadening mechanisms; it may be due in part to density fluctuations within a given size class of silica along with small errors made in the microscopic measurement of particle diameter.) Since the foregoing is only a preliminary treatment of band-broadening effects, a more complete analysis needs to be undertaken in order to resolve the question of whether a density-diameter trend actually exists.

The data provided in Tables V through IX give also average values for the apparent density, pore volume, and porosity. The average values should not be significantly affected by any errors at the extremes of the distribution, which would tend to cancel one another out. While no external data are available for confirming the distributions, the average values can be compared to those measured by other methods. A comparison of average values of these three properties, where available, with the FFF averages are given in Table X. The non-FFF values of Hypersil-5 (support c in Table I) were obtained by BET measurements and were provided to us by Neil T. Miller of PQ Corp. Other non-FFF values were provided by the suppliers. The good agreement in averages found by comparing FFF and non-FFF results provides some confidence in the basic effectiveness of our calibration technique. Obviously, more studies are needed to obtain a better idea of the accuracy of the FFF results.

If we assume that the variation in density across the particle diameter range is negligible (or more accurately that it has

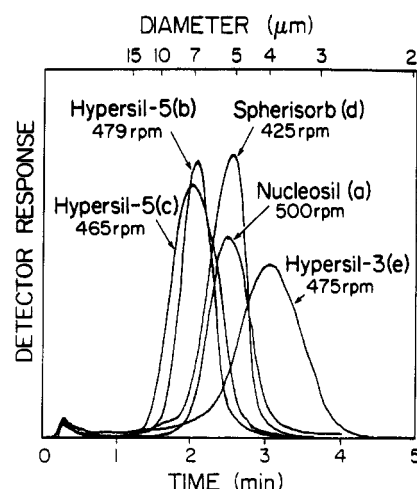


Figure 9. Fractograms of five chromatographic supports used in this study. The rpm for each run has been adjusted to keep the product $G\Delta\rho$ equal.

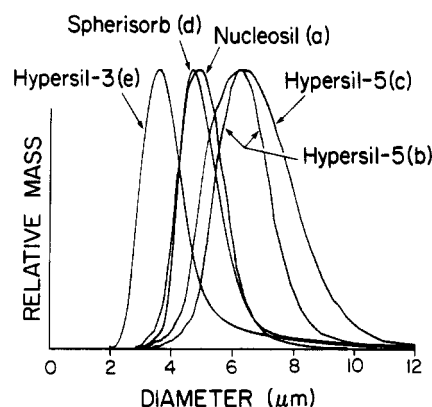


Figure 10. Particle size distributions (plotted to equal heights) of the five support materials based on the fractograms of Figure 9.

negligible effects), then we can adjust the field strength for each of the supports so that they have a common $G\Delta\rho$ product, where $\Delta\rho$ is taken as an average of measured $\Delta\rho$ values for each support (see Table X). A comparison of the fractograms for all five supports at the same $G\Delta\rho$ value ($1.975 \times 10^4 \text{ g/(s}^2 \text{ cm}^2)$) is shown in Figure 9. (This $G\Delta\rho$ value is identical to that of the 1500 rpm plot of Figure 4, which therefore serves as the calibration plot.) Since differences in density are now compensated by an offsetting G value, these fractograms provide a comparative measure of the size distribution of the supports. The diameter scale shown at the top of Figure 9 is obtained from the calibration plot based on polystyrene latex bead retention.

The fractogram of Figure 9 can be readily processed (given the appropriate calibration plot and software) to yield size distribution curves (12). The resulting distribution curves (expressed as relative mass rather than particle number) are shown in Figure 10. While, as suggested above, these size

distribution curves may reflect some inaccuracies if the density varies with size, these inaccuracies should not be large because, first, the density variations, if real, are not large and, second, the effects of these density variations are suppressed by the fact that the diameter-based selectivity is several-fold larger than the density-based selectivity.

CONCLUSIONS

The fact that the sedimentation force depends upon particle density as well as size makes this type of force either advantageous or disadvantageous for use in FFF, depending upon goals. If particle size information alone is desired for a particulate sample, then the dependence of FFF retention on particle density is of little value and may in some circumstances interfere with the acquisition of size data. A density compensation procedure has been developed recently (12) to offset density effects in steric FFF ($d > 1 \mu\text{m}$).

In this paper we extend the density compensation principle one step further by showing that density values for supramicron-size particles can be measured by combining FFF retention data and independent particle size data derived from microscopy or other techniques. This approach is potentially very powerful in that it yields not only average particle density but in some circumstances variations in density with size. This method has the potential to yield much more detailed information than presented here, provided a complete size analysis is performed on each of the fractions collected from the sedimentation FFF run. (Such a size analysis could be done, for example, using flow FFF.) By collection of such data, it is possible that a rather complete characterization of the full size and density distributions of supramicron-size particles could be achieved. This potential wealth of detail concerning particulate materials could be especially valuable for the characterization of complex chemically heterogeneous samples of biological, industrial, or environmental origin.

GLOSSARY

b	channel breadth
d	particle diameter
G	acceleration

L	tip-to-tip channel length
S_d	diameter selectivity
$S_{\Delta\rho}$	density difference selectivity
t_r	retention time
t_{r1}	retention time of 1- μm particle
V	flow rate
V_p	specific pore volume
V_s	specific solid volume
w	channel thickness
ϵ	porosity
$\Delta\rho$	density difference between particle and carrier
ρ	density of carrier
ρ_{app}	apparent density of particle
ρ_p	particle density
ρ_s	density of solid
ρ'	density of fluid in pore space

Registry No. Silica, 7631-86-9.

LITERATURE CITED

- (1) Giddings, J. C. *Chem. Eng. News* **1988**, *66*, 34-45.
- (2) Giddings, J. C.; Caldwell, K. D. In *Physical Methods of Chemistry*; Rossiter, B. W., Hamilton, J. F., Eds.; John Wiley: New York, 1989; Vol. 3B, pp 867-938.
- (3) Giddings, J. C.; Yang, F. J. F.; Myers, M. N. *Sep. Sci.* **1975**, *10*, 133-149.
- (4) Giddings, J. C.; Myers, M. N.; Moellmer, J. F. *J. Chromatogr.* **1978**, *149*, 501-517.
- (5) Giddings, J. C.; Karaiskakis, G.; Caldwell, K. D. *Sep. Sci. Technol.* **1981**, *16*, 607-618.
- (6) Kirkland, J. J.; Yau, W. W. *Anal. Chem.* **1983**, *55*, 2165-2170.
- (7) Nagy, D. J. *Anal. Chem.* **1989**, *61*, 1934-1937.
- (8) Karaiskakis, G.; Koliadima, A. *J. Liq. Chromatogr.* **1988**, *11*, 2863-2883.
- (9) Giddings, J. C.; Myers, M. N. *Sep. Sci. Technol.* **1978**, *13*, 637-645.
- (10) Caldwell, K. D.; Nguyen, T. T.; Myers, M. N.; Giddings, J. C. *Sep. Sci. Technol.* **1979**, *14*, 935-946.
- (11) Koch, T.; Giddings, J. C. *Anal. Chem.* **1986**, *58*, 994-997.
- (12) Giddings, J. C.; Moon, M. H.; Williams, P. S.; Myers, M. N. *Anal. Chem.* **1991**, *63*, 1366-1372.
- (13) Williams, J. C.; Koch, T.; Giddings, J. C. *Chem. Eng. Commun.*, in press.
- (14) Iler, R. K. *The Chemistry of Silica*; John Wiley: New York, 1979; p 478.

RECEIVED for review July 8, 1991. Accepted September 23, 1991. This work was supported by Grant CHE-8800675 from the National Science Foundation.